GJI Geodesy, potential field and applied geophysics

Geophysical investigation and dynamic modelling of unstable slopes: case-study of Kainama (Kyrgyzstan)

G. Danneels,[1] C. Bourdeau,[2] I. Torgoev[3] and H.-B. Havenith[4,*]

[1] *GEO[3]—Applied Geophysics, ArGEnCo Department, University of Liege, Sart Tilman* B52, 4000 *Liege, Belgium. E-mail: gaelle.danneels@ulg.ac.be*
[2] *Itasca Consultants S.A.S., Ecully, France*
[3] *Inst. Rock. Mech. Phys. 'Geopribor', Bishkek, Kyrgyzstan*
[4] *ETH, Zurich, Switzerland*

SUMMARY

The presence of massive Quaternary loess units at the eastern border of the Fergana Basin (Kyrgyzstan, Central Asia) makes this area particularly prone to the development of catastrophic loess earthflows, causing damages and injuries almost every year. Efficient disaster management requires a good understanding of the main causes of these mass movements, that is, increased groundwater pressure and seismic shaking. This paper focuses on the Kainama earthflow, mainly composed of loess, which occurred in 2004 April. Its high velocity and the long run-out zone caused the destruction of 12 houses and the death of 33 people. In summer 2005, a field survey consisting of geophysical and seismological measurements was carried out along the adjacent slope. By combination and geostatistical analysis of these data, a reliable 3-D model of the geometry and properties of the subsurface layers, as shown in the first part of the paper, was created. The analysis of the seismological data allowed us to point out a correlation between the thickness of the loess cover and the measured resonance frequencies and associated amplification potential. The second part of this paper is focused on the study of the seismic response of the slope by numerical simulations, using a 2-D finite difference code named FLAC. Modelling of the seismic amplification potential along the slope confirmed the results obtained from the seismological survey—strong amplifications at the crest and bottom of the slope where there is a thick loess cover and almost no amplification in the middle part of the slope. Furthermore, dynamic slope stability analyses were conducted to assess the influence of local amplifications and increased groundwater pressures on the slope failure. The results of the dynamic modelling, although preliminary, show that a combination of seismic and hydrologic origin (pore pressure build-up during the seismic shaking) is the most probable scenario responsible for the 2004 failure.

Key words: Numerical approximations and analysis; Spatial analysis; Geomechanics; Surface waves and free oscillations; Site effects.

INTRODUCTION

Earthquakes and associated mass movements are common phenomena in tectonically active mountain ranges. One of the most destructive earthquake-induced landslides is the 1970 rock avalanche from Nevados Huascaran, in the Andes of Peru, triggered by the *M* 7.9 earthquake of 1970 and killing more than 18 000 people (Plafker *et al.* 1971). In 1911, a huge earthquake-triggered (M_S 7.6) rockslide (volume about 2 km^3) dammed the Murgab River in the Pamir Range of southeastern Tajikistan, annihilating two villages and creating the Sarez Lake. Another example is the Las Colinas landslide

that occurred in El Salvador, as a result of the *M* 7.6 earthquake in 2001, burying hundreds of houses and people.

The greatest number of deaths caused by earthquake-triggered landslides occurred in the Loess Plateau of China during the 1920 Haiyuan earthquake (*M* 8.5), in which rapid loess flows killed most of the 240 000 people who died in that event (Keefer 2002). Due to its specific microstructure, loess can sustain nearly vertical slopes in dry and non-seismic conditions. However, under strong seismic shaking, this microstructure may break and the loess then behaves as a cohesionless material, creating very rapid loess flows with a long run-out zone (Zhang & Lanmin 1995). The stability of loess slopes is also highly dependent on the water content (Zhang & Lanmin 1995; Derbyshire 2001).

Thus, in case of prolonged rainfalls, loess deposits may suffer subsidence under the influence of medium earthquakes and

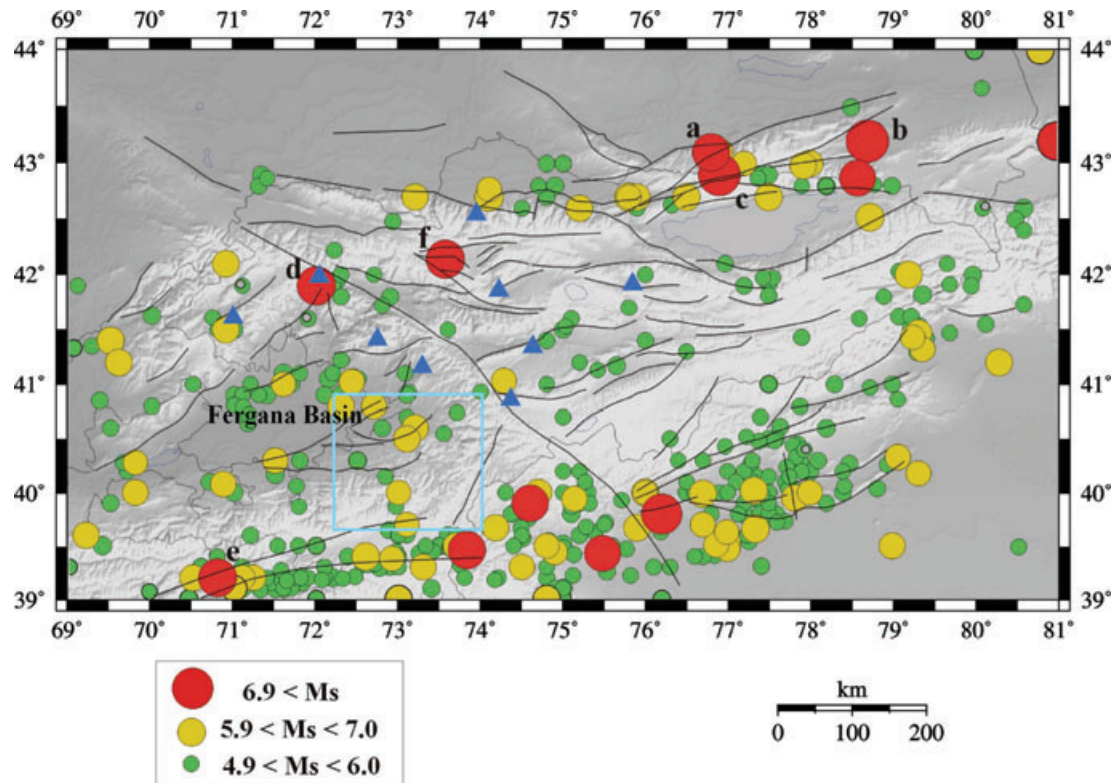*Now at: University of Liege, Belgium

Figure 1. Seismotectonic map of the Tien Shan with indication of location of strong earthquakes that triggered rockslides: (a) *M* 7.3 Verny, 1887; (b) *M* 8.3 Chilik, 1889; (c) *M* 8.2 Kemin, 1911; (d) *M* 7.4 Chatkal, 1946; (e) *M* 7.4 Khait, 1949 and (f) *M* 7.3 Suusamyr, 1992. Blue triangles indicate location of mega-rockslides studied by Strom & Korup (2006). The light blue rectangle outlines the map shown in Fig. 2.

generate large mudflows or floods. This is what happened with many landslides in the Khait region in Tajikistan during the M_S 7.6 Khait seismic event (1949). In particular, this earthquake triggered a large rockslide (see 'e' in the map of Fig. 1), which was transformed into a highly mobile rock avalanche—loess flow by the entrainment of a large amount of saturated loess from the slopes and valley floor. The mass movement ran-out a distance of 11 km, burying two towns with an estimated loss of 15 000 people (Leonov 1960; Keefer 2002).

The loess terrains of China, located between the Tibetan Plateau in the southwest and deserts in the north and west, represent the highest accumulations of loess over the world, with a maximum thickness up to 500 m in Northern China (Derbyshire 2001). This is due to the juxtaposition of high mountains with frost action and deep desert basin. Thick loess deposits are also found all over Central Asia (Kazakhstan, Uzbekistan, Kyrgyzstan and Tajikistan) at the limit between the mountain regions and sand and stone deserts (Dodonov 1991; Pye 1995).

KYRGYZSTAN

In the northern part of Kyrgyzstan, numerous large rockslides have been triggered by strong earthquakes. Havenith *et al.* (2003) describe seismically triggered rockslides following the 1885 Belovodsk earthquake (*M* 6.9), the 1911 Kemin earthquake (*M*$_S$ 8.2) and the more recent 1992 Suusamyr earthquake (*M*$_S$ 7.3). Strom & Korup (2006) have examined nine large-scale rockslope failures (see blue triangles in the map of Fig. 1), most of them

located on or near active faults. They support the hypothesis that strong seismic shaking is the main cause of these rockslides. Most of these mass movements occurred in remote areas and therefore did not create large damage. The region with highest concentration of landslides is located along the eastern rim of the Fergana Basin, surrounded by high mountain ranges (see location in Figs 1 and 2). Since this region is densely inhabited, the mass movements regularly cause damage to settlements and are responsible for a yearly loss of more than 30 human lives. The majority of these landslides occur in form of rotational slides in weakly consolidated Quaternary and Tertiary sediments (Roessner *et al.* 2005).

In this region, the landslides are generally not directly triggered by earthquakes, rather by a complex interaction of seismic, tectonic, geological and hydro-meteorological factors (Havenith *et al.* 2006). One example of landslide occurrence linked to a seismic event is the movement (about 0.5 m) of the Upper Koytash landslide in the Maily-Say area registered on 1997 January 9. At the same time, a M_S 5.9 earthquake was recorded at an epicentral distance of 150 km from the site. Other failures could be interpreted as post-seismic displacements. The main movement of the Tektonik landslide (Maily-Say) in 1992 July occurred seven weeks after a M_S 6.2 earthquake located at an epicentral distance of 30–35 km.

Along the eastern rim of the Fergana Basin, the predominant type of landslides is related to the presence of massive Quaternary loess units, up to 50 m thick (Roessner *et al.* 2005). These loess landslides of the Southern Kyrgyz Provinces cause damage to settlements and infrastructure and cause injuries almost every year. Therefore, one of the major concerns in this area is the development of risk management related to mass movements. Efficient disaster management
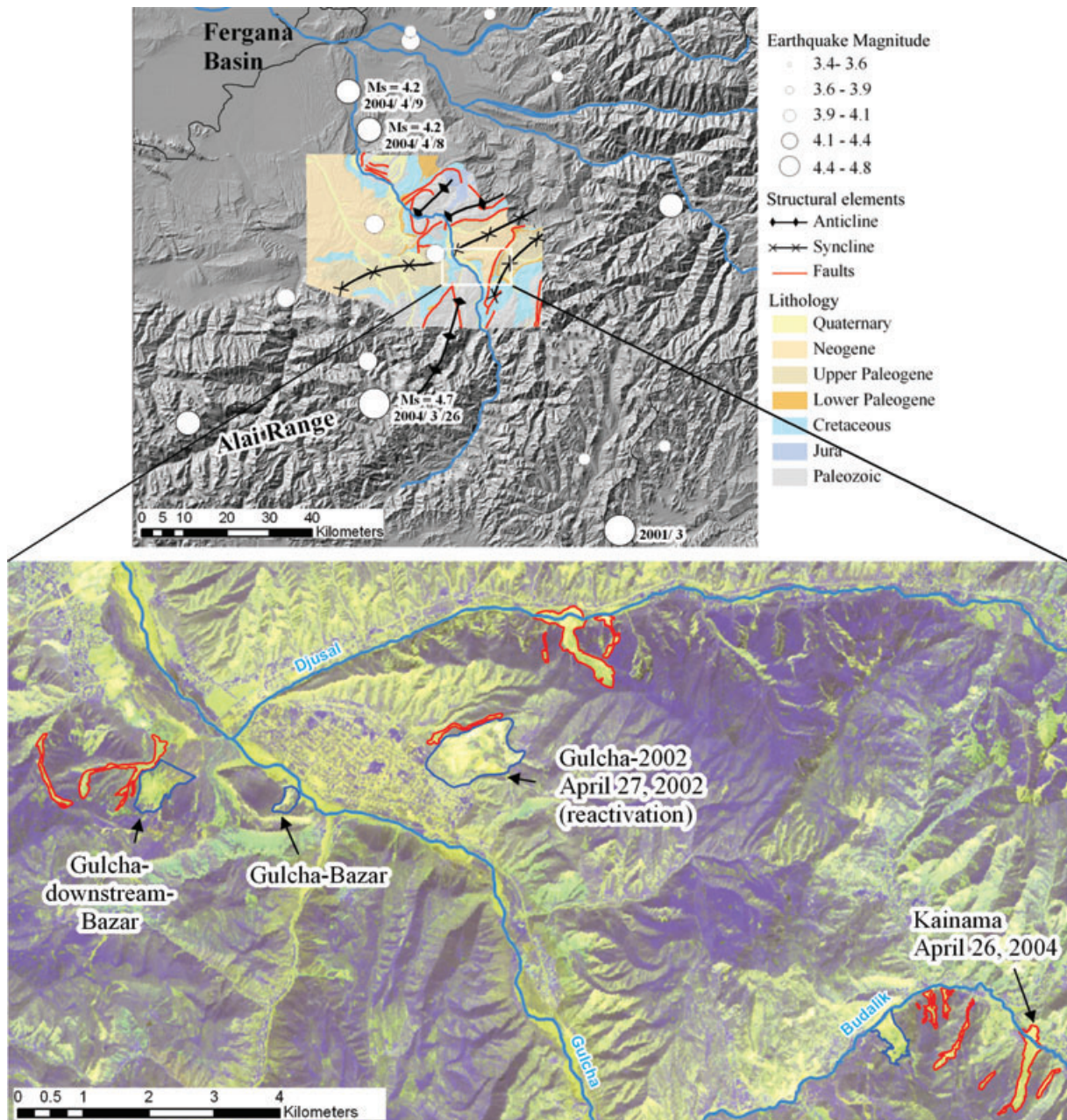
Figure 2. (a) Shaded relief map of the southeastern rim of the Fergana Basin, with location of recorded earthquakes (*M* > 3.4, from 2000 to 2004) and geological map around the Gulcha town. (b) ASTER image (VNIR bands, 2004 May) covering the Gulcha study area with indication of earthflows (in red) and earthslides (in blue).

and mitigation requires a good understanding of the causes of mass movements: heavy rains and associated groundwater pressure and earthquake shocks. During the summer 2005, several sites around the Fergana Basin with existing and/or initiating slope failures and a high potential of seismic (re)activation have been studied in detail. Geophysical–seismological data have been recorded in three main sites, Kainama, Taran-Bazar and Maily-Say, located in Southeastern, Eastern and Northeastern Fergana, respectively (see Fig. 2). In Kainama, a fatal loess earthflow occurred in 2004, preceded by relatively small-magnitude earthquakes and heavy rain falls. This site has been chosen as pilot area for further investigation. The final goal was to assess the seismic amplification potential of the layers

and the influence of the amplification and increased groundwater pressures on the slope failure using numerical modelling. Geophysical and seismological measurements were carried out along the eastern adjacent slope of the existent loess flow, considering that the conditions are very similar.

In the first part of this paper, a reliable model of the geometry of the subsurface layers (and in particular of the upper soft sediment layers) and their properties is created by combination of the geophysical and seismological data and geostatistical analysis. The second part of the work is focused on the numerical simulations of site effects and slope stability under seismic conditions considering hydro-mechanical coupling.

LOESS EARTHFLOWS AND SLIDES IN THE GULCHA REGION

The Gulcha region is located in the transitional zone between the Fergana Basin in the north and the Alai Range in the south, with elevations ranging from 1500 m in the Gulcha village up to 4000 m in the surrounding mountains. The area is characterized by a moderate to high seismic hazard, with an average 'peak ground acceleration' level of 0.3–0.4 g (Abdrakhmatov *et al.* 2003). Fig. 2(a) shows all registered earthquakes during the period from 2000 to 2004 within a radius of 50 km around the village of Gulcha. The tectonic structure is quite complex, including anticlines and synclines, as well as upthrust faults (see Fig. 2). The region is composed of Palaeozoic and Cretaceous rocks in the anticlines, whereas the synclines contain a succession of weakly consolidated clay and limestone of the Palaeogene and Neogene. The river valleys are filled with Quaternary deposits. Most of the rocks of this area are covered by a mantel of loess (not represented on the geological map) with a thickness up to 10–15 m (internal report of the Kyrgyz Ministry of Environment and Emergency, MEE).

The presence of loess is a very important factor for this area. Indeed, over a surface area of 150 km^2 around the village of Gulcha, about 15 big landslides (20 000–950 000 m^2) developed in loess during the last 10 yr (Fig. 2b). Two main types of landslides can be differentiated: most of the detected mass movements are elongated earthflows made only of loess (outlined in red). The remaining slope failures are earthslides, which also involve the underlying bedrock in the failure process (outlined in blue). Derbyshire (2001) extensively studied the landslides in the loess plateau of Northern China and proposed a classification of the loess landslides, based on the composition of the sliding material and the localization of the failure plane. According to this classification, the earthslides are defined as 'mixed landslides', which involve mixtures of loess and bedrock and are sliding along bedding or joints of the bedrock.

The loess earthflows can further be differentiated according to the location of the failure plane (Derbyshire 2001): 'bedrock contact landslides', 'palaeosoil contact landslides' and 'slides within loess'. The first two types of sliding involve the sliding of the loess mass along a less permeable (or even impermeable) horizon. During prolonged rainfalls, a zone of saturation can build up along this less permeable surface, which results in a reduction of the soil shear strength. The velocity of sliding of these two types of loess earth flows can be very rapid, reaching several metres per second (internal report of MEE). 'Slides within loess' are less common in China and usually require the occurrence of an earthquake shock or the undercutting of the slope (Derbyshire 2001).

The 'Kainama' earthflow (220 000 m^2) developed on 2004 April 26 and caused the destruction of 12 houses and the death of 33 people (64 families became homeless). This landslide formed within the loess layer and developed into a very rapid flow with a long run-out zone: the involved mass travelled over a distance of 1000 m on the southern flank, crossed the river and went up on the opposite flank over a distance of 250 m. Fig. 3 shows the evolution of this landslide from 2001 to 2004. In 2001, no clear sign of instability is seen (see Fig. 3a). In spring 2003, several cracks appeared on the upper part of the slope (internal report of MEE). From the photograph in Fig. 3(b) dated 2003 August, it can be seen that a small part of the slope (about 5000 m^2) is already sliding and denuded of vegetation. The main failure of 2004 April (Fig. 3c) was preceded by an increased seismic activity: on 2004 March 26, an earthquake of M 4.7 occurred 40 km SW of the Kainama site (see Fig. 2a). Two other earthquakes were registered some 50 km NW of Kainama on 2004 April 8 (M 4.2) and April 9 (M 4.2). The rise of the groundwater level after spring rains and snow melting (indicated by the presence of spring along the slope) also played an important role for the landslide formation. During our fieldwork during summer 2005, several new cracks were visible on borders of the landslide which indicates a probable reactivation.

GEOPHYSICAL–SEISMOLOGICAL INVESTIGATION

Due to its remote location and the very sudden and recent occurrence, the Kainama slide was very poorly documented. During summer 2004, a first study was conducted by a team of Kyrgyz experts in the framework of a 'natural disaster mitigation project' at national level, consisting of a brief description of the geometry and the probable causes of the landslide. However, an effective landslide risk management is only possible with a clear understanding and modelling of the geometry, behaviour and dynamics of the landslides. To this end, an extensive geophysical–seismological survey has been carried out in summer 2005 by a collaboration of Kyrgyz,
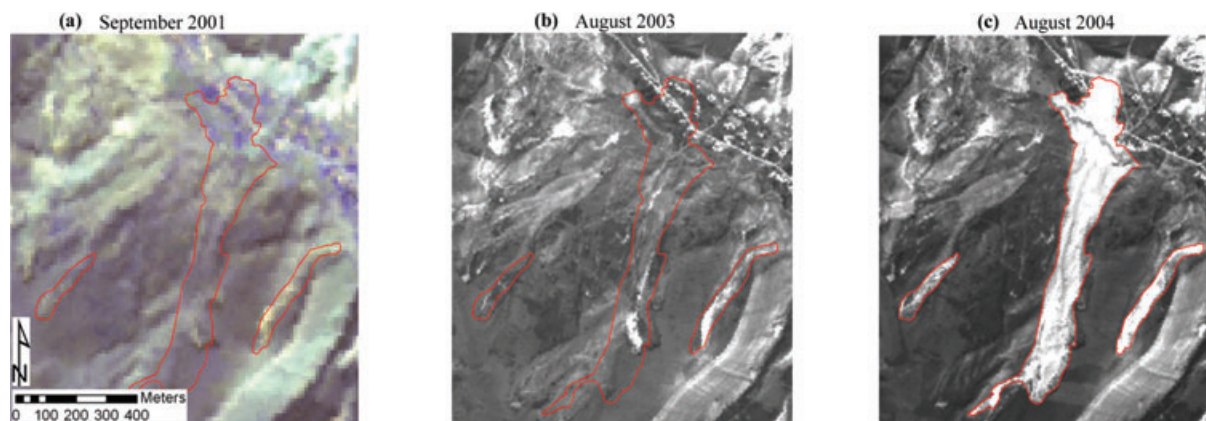

Figure 3. Evolution of Kainama and adjacent loess flows. Red contours indicate extent of fully developed landslides. (a) ASTER image (VNIR bands) dating of September 2001—no clear sign of instability; (b) SPOT 5 image dating of August 2003– small parts are denuded and sliding and (c) SPOT 5 image dating of August 2004—final extend of landslides after failure of 2004 April 26.
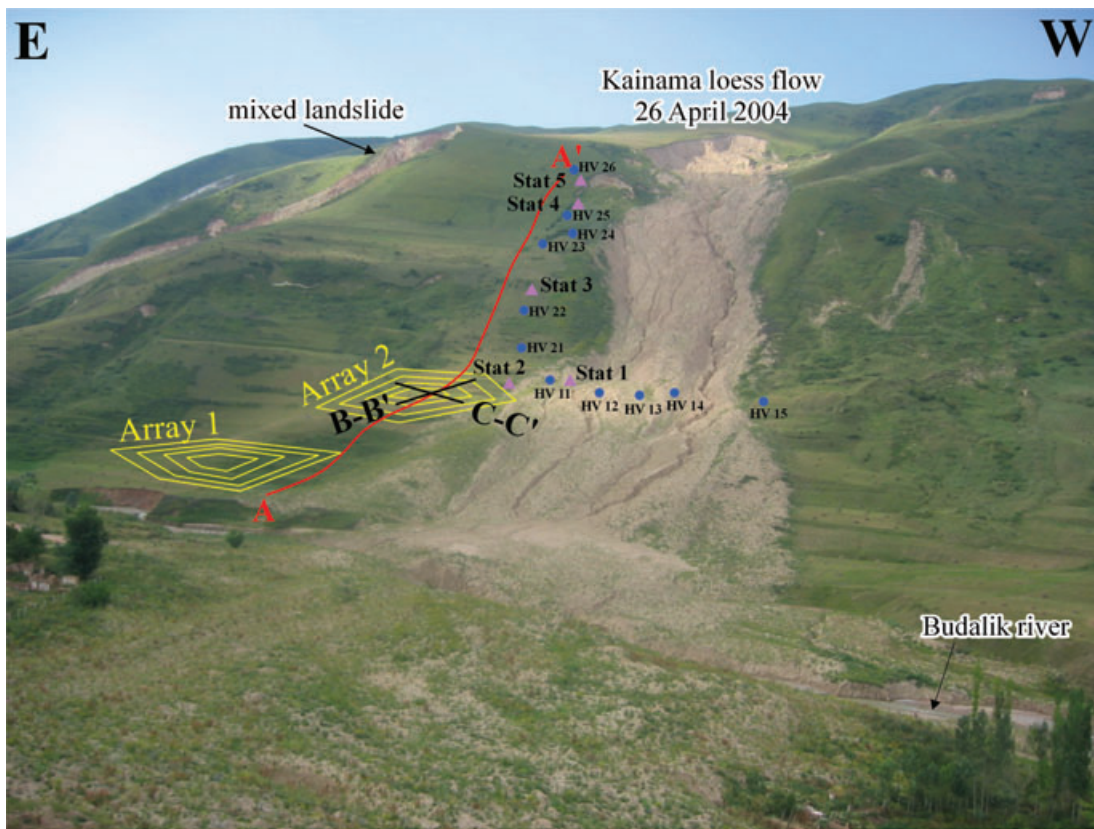
Figure 4. Investigated slope in Kainama—geoelectric profile (red), arrays (yellow), seismic tomography profiles (black), earthquake recordings (purple triangles) and *H/V* measurements (blue dots).

Swiss and Belgian teams. Most of the measurements were carried out on the eastern adjacent slope of the existent loess flow (see Fig. 4). Considering that the conditions are very similar, the obtained results of subsurface structure and properties can be used for the analysis of the failed slope.

The survey included electrical resistivity tomography (profile A–A′ in Fig. 4), seismic refraction tomographies (B–B′ and C–C′), earthquake ground motion recordings (Statx) and ambient noise measurements using the array method (Array1 and 2) and the *H/V* single station method (HVxx). Recent studies have shown that these methods provided good results for delineating the landslide mass and detecting (potential) failure planes (Perrone *et al.* 2004; Lebourg *et al.* 2005; Jongmans & Garambois 2007; Meric *et al.* 2007). The combination of different methods also allows us to validate the results and to check their reliability.

Seismic noise measurements

Seismic noise measurements are relatively cheap and simple methods making use of the natural ground vibrations (microtremors). The spectral ratio of horizontal to vertical components (*H/V* ratio) and the seismic arrays are the two main noise techniques. The *H/V* ratio technique is nowadays a widely used method to estimate the resonance frequency of a soft sediment layer (for more details see Faeh *et al.* 2001, among others). In case of a single homogeneous soft layer covering a stiffer layer and knowing an estimate of the shear wave velocity V_S, this fundamental frequency f_0 can be linked to the thickness h of the layer by the equation $f_0 = V_S/4h$.

H/V single station measurements were acquired along two profiles, in EW and NS directions (see Fig. 4). The natural ground vibrations were recorded during 20 min (250 Hz sampling frequency) with a Lennartz 5 s 3-D sensor connected to a seismic station produced by the Swiss Seismological Service. The recordings were processed with the GEOPSY software produced by Wathelet (2005). For each horizontal component, *H/V* ratios were averaged for more than 20 time windows of a length of 10–20 s ($AvHV_{NS}$ and $AvHV_{EW}$). Combining the NS and EW components the final *H/V* was computed by $\sqrt{(AvHV_{NS})^2 + (AvHV_{EW})^2}$.

Figs 5(a) and (b) show *H/V* ratios for the two profiles (including the *H/V* measurements acquired with the earthquake ground motion recordings). Along the horizontal profile (EW-oriented), all fundamental frequencies have similar values between 4 and 6 Hz (but with significantly larger peaks obtained in the east of the landslide). On the contrary, the fundamental frequency strongly varies along the NS-oriented slope profile; it is about 6 Hz in the lower part of the slope, 10–15 Hz in the middle part (if a peak is visible) and about 4 Hz in the upper part of the slope. The recordings of the earthquake recording stations and of the arrays were also used to derive *H/V* ratios. Based on the picked fundamental frequencies, the thickness of the loess layer was determined using the above-mentioned formula, considering a mean V_S velocity of 180 m s^{-1} (defined by the seismic arrays, see below). The spatial variation of the calculated loess thickness is displayed in Fig. 5(c). This analysis shows that the loess layer has an average thickness of 10–12 m in the lower and upper part of the slope, and a thickness of 3–6 m in the middle part.
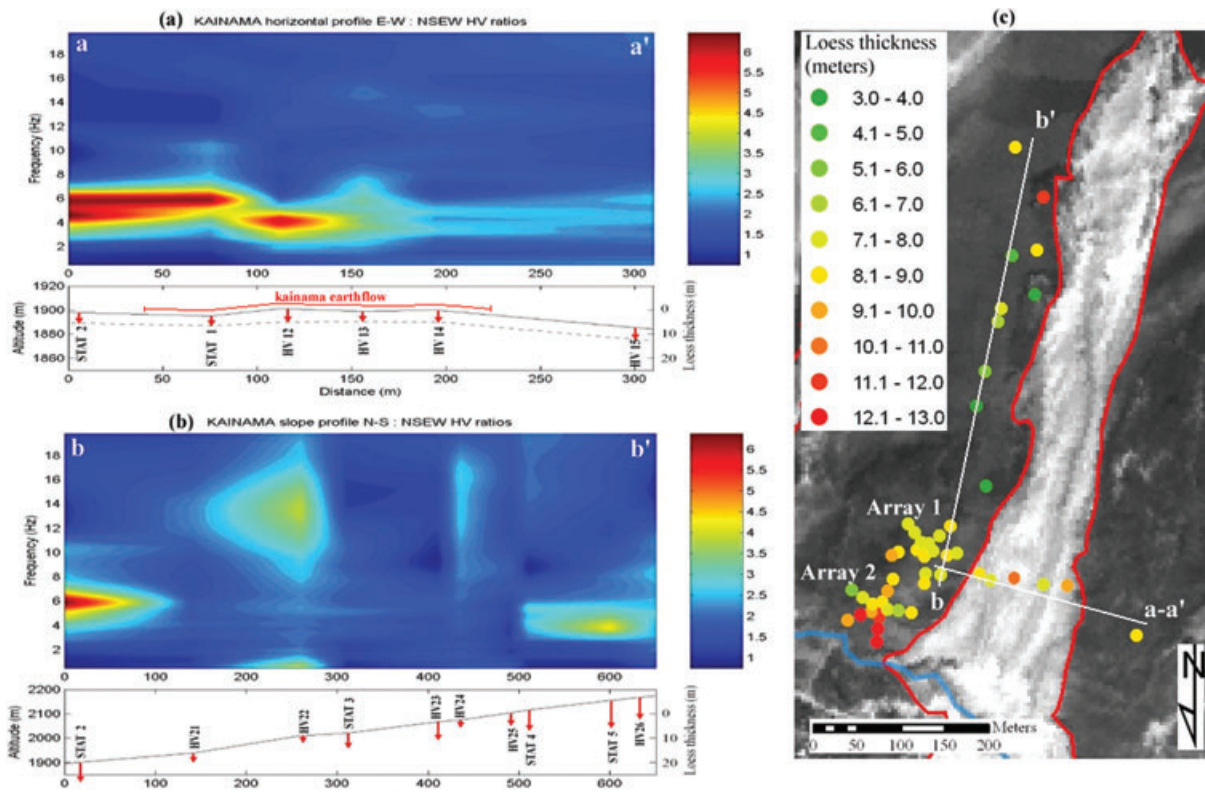
Figure 5. *H/V* ratios along the horizontal (a) and slope (b) profile with indication of the loess thickness with red arrows. The vertical colour scale bar represents the amplitude of the *H/V* ratios. (c) Spatial variation of the calculated loess thickness.

The array technique is a more complex technique, based on wave time delay measurements between coupled stations. This method allows for defining the dispersion curve of the Rayleigh-wave phase velocity and thus, to derive subsurface shear wave velocity profiles. Two arrays measurements (A1 and A2) were performed at the base of the slope (see Fig. 4), consisting of four rings in regular pentagonal configuration: five stations successively installed at a distance of 5, 12, 30 and 50 m from the central station. For each ring about, 1 hr of noise data were recorded (less for the smaller rings, more for the larger ones).

The records of each 'subarray' were analysed with the high-resolution beam forming frequency–wave number (*F–K*) method developed by Capon (1969). The dispersion curve was determined by the maximum energy within the *F–K* spectrum. The processing was done with CAP (Ohrnberger 2004), which is part of the GEOPSY package (Wathelet 2005). From the corresponding four subarray dispersion curves, we extracted relevant parts, between aliasing at high frequencies and loss of resolution at lower frequencies, and connected them with each other (the selection of the parts is described in detail in Havenith *et al.* 2007). Once dispersion curves are joined, the combined curve is used as input for the determination of the *S*-wave velocity model through data inversion. The inversion processing was done with the software included in the GEOPSY package (na-viewer developed by Wathelet *et al.* 2004 using the neighbourhood algorithm).

Both *S*-wave velocity (V_S) models indicate a shear wave velocity of about 180 m s^{-1} for the upper loess layer and a depth of 8 m for Array1 and 6 m for Array2, which is in good agreement with the thickness values derived from the *H/V* measurements. On both profiles, a second layer is characterized by a $V_S = 400$–600 m s^{-1}.

Electrical resistivity tomography

The electrical resistivity tomography is a widely used method to study resistivity variations of the subsurface, which can be caused by several factors: lithological changes, the degree of weathering and the presence of groundwater. One electrical tomography profile of a length of 840 m was recorded along the roughly NS oriented slope (see Fig. 4). A Schlumberger configuration and an electrode spacing of 5 m were used. The data were processed with the 2-D inversion algorithm proposed by Loke & Barker (1996) to obtain a resistivity section.

This section is shown in Fig. 6, with indication of the loess thickness inferred from *H/V* measurements. A clear contrast can be observed between the surficial layer(s) with resistivity values of less than 200 ohm-m and the stable bedrock with values of 300–1200 ohm-m. The bedrock interface can be delimited at a depth of 30–50 m. In the upper layer, zones with very low values (less than 20 ohm-m) probably indicate the presence of water-saturated parts. These zones are not continuous along the surface. The lowest resistivity values are observed in the valley close to the river at a depth of 20 m (below the alluvial layer) and in the upper part of the slope at very shallow depths (within the loess). At the upper limit of this latter zone (at a distance of 700 m along the electrical tomography in Fig. 6), a new landslide scarp is forming, just on top of the shallow bedrock marked by the presence of high resistivities at 20 m depth. The low resistivity zone at different depths along the surface is attributed to the presence of more clayey (but compact) materials at the bottom of the loess layer. This impermeable layer is likely to induce a perched water table within the loess layer in the upper part of the slope.
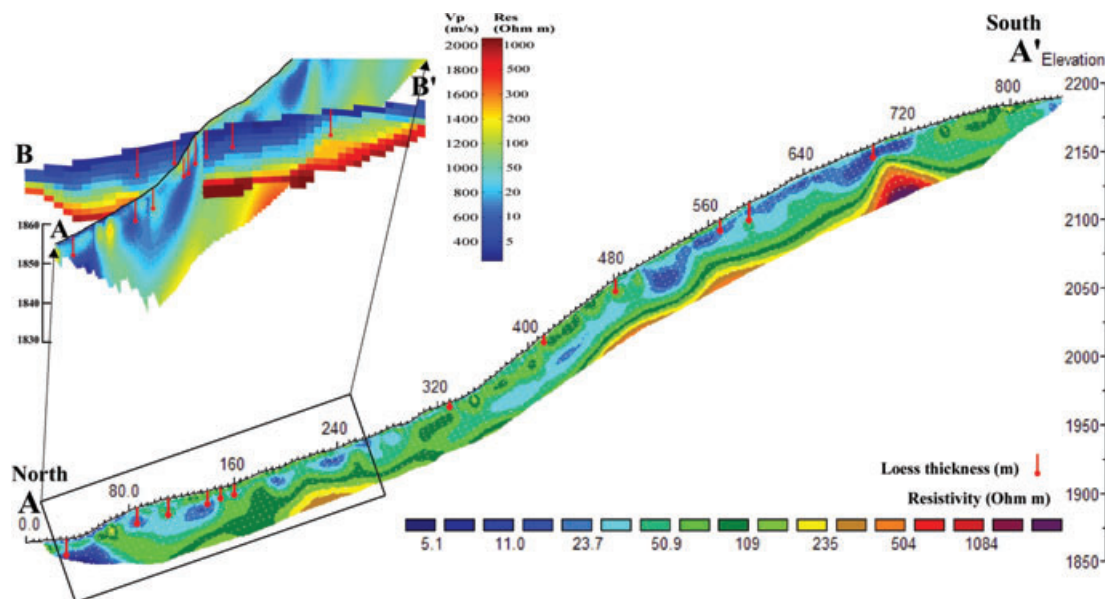
Figure 6. Electric resistivity profile along the slope: surficial layers (upper loess layer and weathered bedrock) with low resistivity values (<200 ohm-m), stable bedrock with high resistivity values (300–1200 ohm-m). Thicknesses of loess (and alluvia at left-hand side valley bottom) derived from *H/V* measurements are represented by red colons. (zoom) Intersection of resistivity and seismic tomographies of the surficial layers (upper loess layer and weathered bedrock). The increase of V_P velocity indicates an increase in compaction.

Seismic refraction tomography

The seismic tomography is based on the inversion of the first-arrival time of seismic signals and allows obtaining a 2-D image of the *P*-wave velocity distribution of the subsurface. Two seismic refraction profiles of a length of 57 m (B–B′ and C–C′) were carried out at the base of the slope (see Fig. 4). The profiles included 12 geophones with a spacing of 3 m, 3 sledge-hammer shots (at the two ends and the centre) within the 33 m long profile and 3 offset shots at both ends at distances of 3, 6 and 12 m. The picked *P*-wave arrival times were processed by the seismic refraction tomography software SARDINE developed by Demanet (2000).

The two resulting seismic images show similar results (only profile B–B′ is shown in Fig. 6) and are characterized by a gradually increase of V_P velocity with depth. The upper 6 to 8 m, which correspond to the upper loess layer (see zoom of Fig. 6), are defined by *P*-wave velocities of 300 to 800 m s^{-1}. In the lower 10 to 20 m, V_P values are ranging between 1000 and 1800 m s^{-1}, indicating an increase in compaction with depth (and likely partial water saturation). This layer will further be defined as weathered bedrock.

Earthquake ground motion recordings

Earthquake ground motions were recorded at four sites along the slope (Stations 2–5, see Fig. 4) and one site (Station1) on the Kainama landslide. During four nights, 12 local earthquakes (small epicentral distances, magnitudes unknown) were recorded at each station. Station1 has been used as reference station (selected due to lowest position along the slope, the loess thickness there is 8 m) for the computation of the spectral ratios (*SR*—not standard since the reference station is not on rock), that is, the ratio of the Fourier spectra of the *S*-waves of all stations (2–5) over the spectra of reference station for the same time-windows. These ratios define the amplification potential of the studied location compared with the reference site (the absolute amplification with respect to a bedrock site could not be determined). The mean *SR* profile along the slope is displayed in Fig. 7, which shows a correlation with the thickness of the loess layer: strong amplifications at the upper and lower parts of the slope with a thick loess cover, and small amplifications with higher resonance frequencies in the middle part. The strongest amplification with a factor of 6 is found at the crest of the slope, for a frequency of 6 Hz.

3-D GEOPHYSICAL MODEL

For accurate seismic ground motion simulations and slope stability computations, a reliable 3-D geophysical model of the subsurface is required. The surface of this 3-D model is a filtered and georeferenced Digital Elevation Model (DEM) created from a topographic map of scale 1:25 000. This DEM, with a 15 m pixel resolution, is a 'surfometric' model, that is, for each pixel of the grid, the longitude and latitude coordinates, as well as the elevation of the surface are defined.

By processing and combining the results from the geophysical–seismological survey, this surfometric model is upgraded to a complete geological–geophysical 3-D model. Thus, for each pixel of the grid, information about the thickness of the different geological layers and their geophysical–seismological properties are added.

Using the results of the survey, a model composed of three layers is defined: the loess layer, an intermediate layer of weathered bedrock and the bedrock. The thickness of the loess layer could be determined in each measurement point of seismic noise (*H/V* single stations, earthquake recordings, arrays). By analysing these data, a correlation is observed between the thickness of the loess layer and the steepness of the slope—the upper and lower parts of the flank (with lower slope values) are characterized by thicknesses of 10–12 m, whereas the steeper middle part shows lower thicknesses (4–6 m).

The depth data from all these measurements points were used for interpolation to define the loess thickness over the entire study
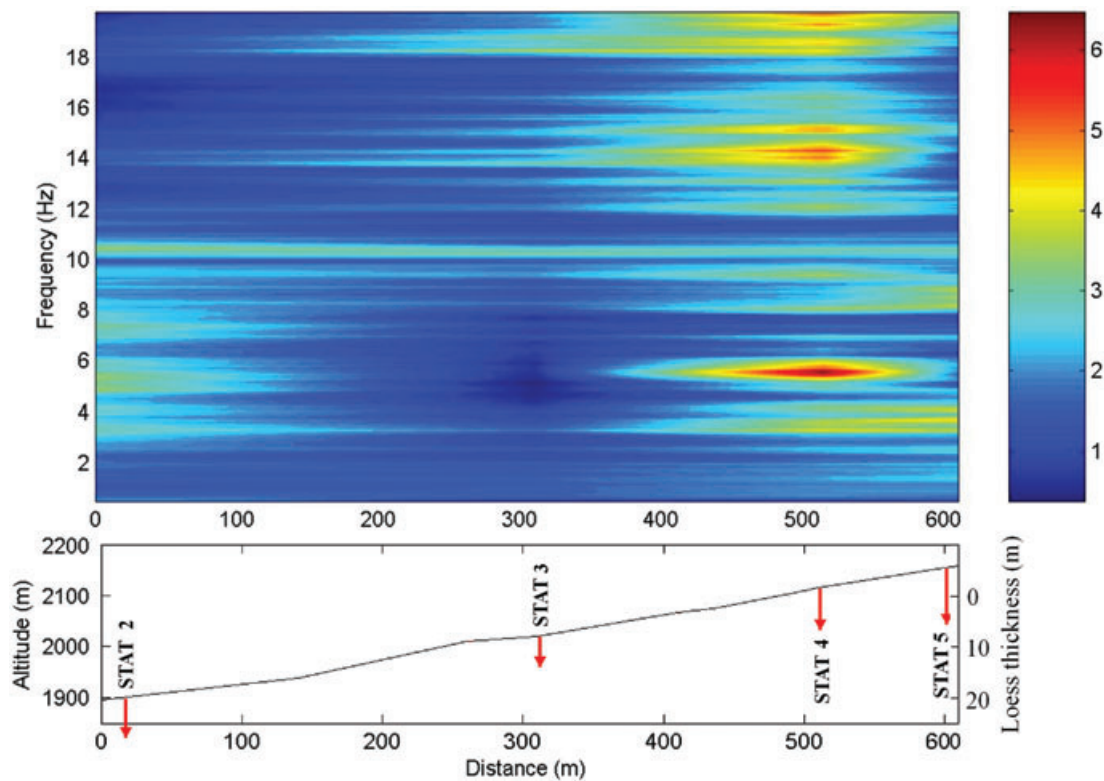
Figure 7. Mean spectral ratio (average over NS and EW component) profile of the earthquake ground motion recordings along the slope with indication of loess thickness (red arrows).

area (Fig. 8a). Having not enough samples for the probabilistic kriging method, the deterministic inverse distance weighting (IDW) method was used for the interpolation. To make it possible to take the thickness–steepness correlation into account, the distance factor can be defined in a normalized multivariate state space. In this case, the distance factor has been defined as a function of the planimetric distance and the elevation, thus including indirectly the steepness of the slope. The same concept was applied for creating the middle layer, using the information of the geoelectric profile for defining the interface between the middle layer and the bedrock.

Finally, information on V_S, V_P and resistivity data of the different layers was included to create a complete 3-D geophysical model (Fig. 8b): the loess layer is defined by low V_S (180 m s^{-1}), V_P (500 m s^{-1}) and resistivity ($<$200 ohm-m) values (it should be noted that this layer corresponds to alluvia with similar seismic properties in the valley bottom); the middle layer, weathered bedrock by intermediate values; the bedrock by high V_S ($>$1400 m s^{-1}), V_P (2500 m s^{-1}) and resistivity ($>$300 Ohm m) values.

NUMERICAL MODELLING

Creation of a 2-D model

Gathering all the information presented in the previous paragraphs, we created a numerical model to study the seismic response of the slope eastern adjacent to the existing loess slide. As shown in Fig. 4, the Kainama landslide originated from an EW elongated rim that can be considered as infinite in this direction (length of 1.5 km). A 2-D cross-section, parallel to the principal direction of mass movement (NS) was extracted from the 3-D geophysical model displayed in Fig. 8. We used the 2-D finite difference code FLAC (Itasca

2005) to generate a grid adapted to the desired shape (Fig. 9). Its layering and elastic properties were derived from field measurements (see paragraph 4 for further details), whereas its strength parameters come from a literature review of other loess sites (Derbyshire 2001). As shown in Table 1, summarizing material properties, the loess layer was subdivided into two units according to their clay contents: the superficial layer is made of sandy loess deposits, and it is underlain by a clayey loess layer. This latter layer is not present in the 3-D model shown above (there, it is part of the weathered bedrock layer) since its thickness is not constrained by the H/V measurements (showing the thickness of the upper low-velocity sandy loess layer). Therefore, its extension outside the profile is not known. Along the profile, it is marked by lower resistivities (than the surficial loess and the weathered bedrock) and larger average P- and S-wave velocities (than the surficial loess but slightly lower than those of the weathered bedrock). Since the likely presence of clay is important for (dynamic) stability computations (including changes of groundwater pressures), it has been represented in the 2-D model shown in Fig. 9, considering that the extension of this layer is poorly constrained as discussed later.

In FLAC software, the model is divided into a finite difference mesh composed of quadrilateral elements or zones. The smallest zones in the model, along with the stiffest materials, determine the dynamic time step (and consequently computation times). Kuhlemeyer & Lysmer (1973) showed that for accurate representation of wave transmission through a model, the element size must be smaller than approximately 1/10 to 1/8 of the wavelength associated with the highest frequency component of the input wave. In the lack of ground-motion recordings of the sequence of earthquakes that preceded the triggering of the landslide, numerical simulations were performed with a synthetic seismic signal applied along the
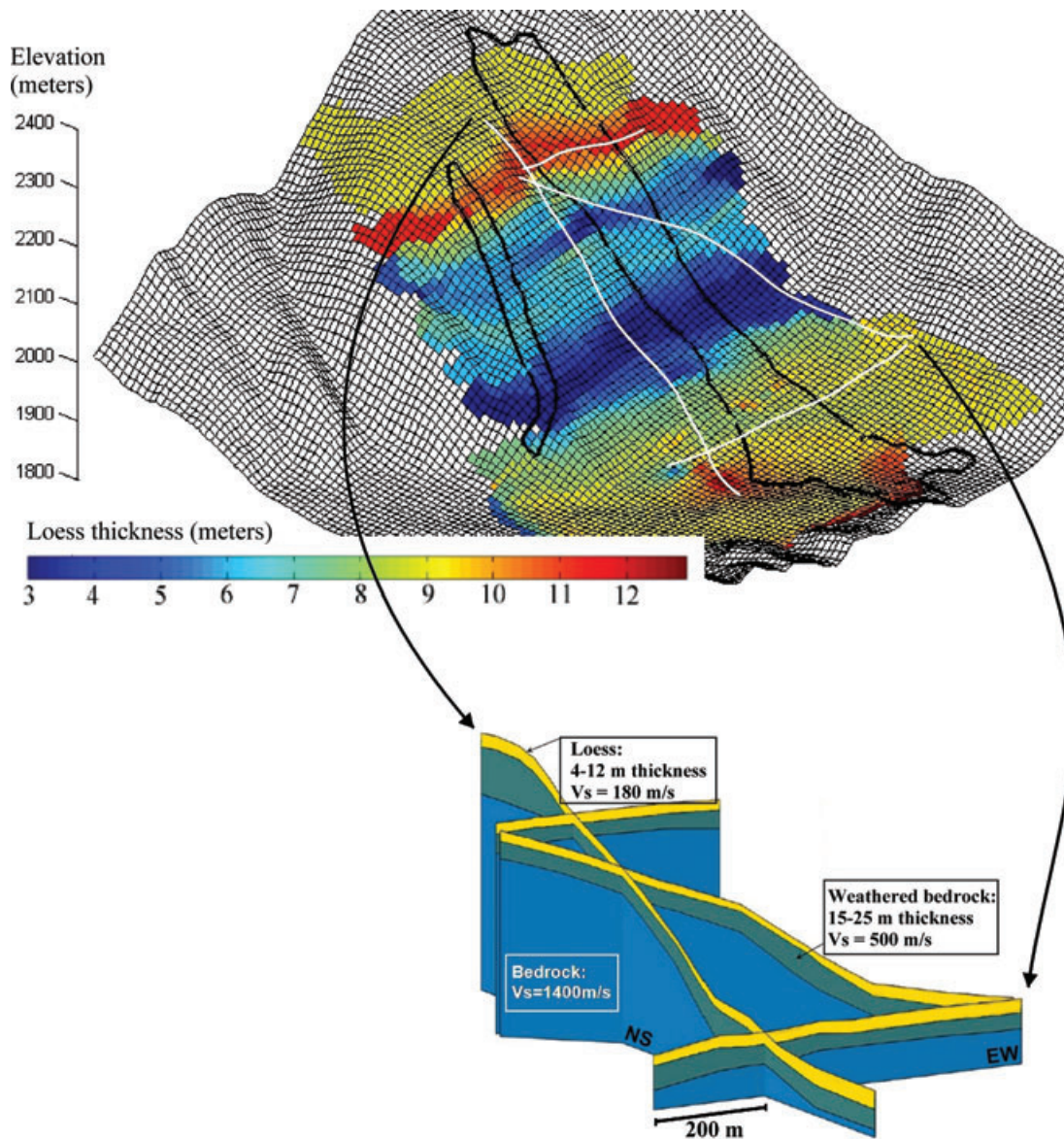
Figure 8. (a) Digital elevation model with the interpolated thickness of the loess layer (metre) using the IDW method with indication of the location of cross-sections (white lines) shown in (b). (b) Sections across the 3-D geophysical model.
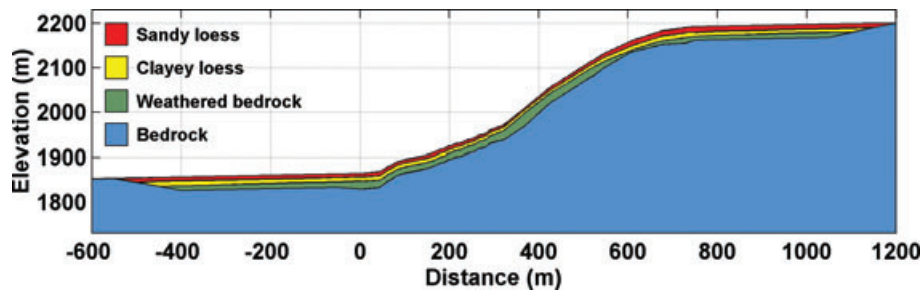

Figure 9. 2-D cross-section of the Kainama slope.

base of the model. This signal is a plane elastic *SV* wave, propagated vertically towards the surface and polarized horizontally (the *SH* case is not studied here). We used a sum of two single Ricker wavelets with a maximum amplitude of 0.025 *g*, a total duration of 5 s (with approximately 0.4 s of strong motion) and a frequency band ranging approximately from 2 to 8 Hz (Fig. 10). The amplitude of 0.025 *g* is half of the maximum value that could have been recorded on a rock surface during one of the earthquakes preceding

Table 1. Material properties of all layers constituting the Kainama slope.

	Dry density (kgm^{-3})	S-wave velocity (m s^{-1})	P-wave velocity (m s^{-1})	Poisson's ratio	Cohesion (kPa)	Friction angle (°)
Sandy loess	1500	180	400	0.37	45	32
Clayey loess	2000	400	900	0.38	45	28
Weathered bedrock	2100	600	1500	0.40	150	34
Bedrock	2300	1400	2500	0.27	200	35
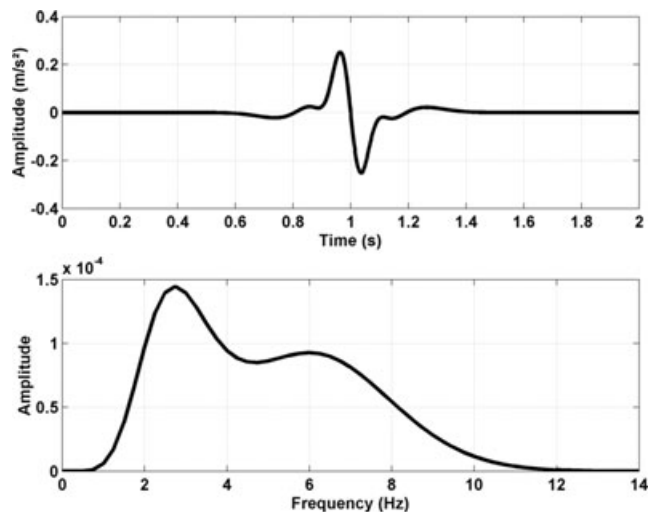
Figure 10. (top) Synthetic signal applied along the base of the model and (bottom) its Fourier amplitude spectrum.

the mass movement in 2004 April. The duration has been chosen arbitrarily whereas the frequency band was selected to cover the resonance frequencies of the site.

Considering the increase of *P*-wave velocity with depth, we created a zoning with a fine mesh in the region of interest close to the surface to a coarse mesh near the boundaries. The element size was set to 1 m in the region of interest (800 m wide region with a maximum thickness of 50 m located below the ground surface) to allow the propagation of frequencies up to 8 Hz. For reasonable accuracy, the ratio between adjacent zones was kept smaller than 4 : 1 and the aspect ratio of zone dimensions did not exceed 5 : 1.

To prevent the reflection of outward propagating waves back into the model, an absorbing quiet boundary (Lysmer & Kuhlemeyer 1969) was applied along the base of the model. To minimize wave reflections along the lateral boundaries and to achieve free-field conditions, a 1-D free-field grid was coupled to the main grid by viscous dashpots to simulate quiet boundaries (Cundall *et al.* 1980). Since this method is not perfect for low angles of incidence (<30°) and for surface waves, we placed the boundaries of the model at some distance from the region of interest to minimize the effect of reflected waves. The model is 2100 m wide and 470 m high; it contains approximately 166 000 zones with sizes ranging from 2 m × 6 m close to the boundaries to 1 m × 1 m below the ground surface. Attenuation of seismic wave energy in a soil, subjected to dynamic loading, is reproduced by Rayleigh damping in the FLAC code (Itasca 2005). In the lack of any constraint on damping in Kainama site (attenuation of surface waves was not studied), a small percentage of damping (3 per cent) centred on the natural frequency of the site (3.5 Hz) was applied to the model.

The general calculation sequence embodied in FLAC is composed of two main parts executed every time step to update all of the grid variables. First, the equations of motion are invoked to derive new velocities and displacements from stresses and forces (gravity forces and seismic shaking in the present case). Then, strain rates are derived from velocity gradients, and new stresses are determined from strain rates using the constitutive relation or stress–strain law. Neighbouring elements cannot affect one another during one time step, but, after several cycles, disturbances propagate across the grid.

Modelling of site effects

The first goal of the modelling was to assess the seismic amplification potential of the layers for a qualitative comparison with mean *SR*, displayed in Fig. 7. We calculated spectral amplifications along the surface by dividing the Fourier amplitude spectra of the computed horizontal signals by the Fourier amplitude spectrum of the reference horizontal motion (input with doubled amplitudes simulating ground-motions recorded on a rock site): the results are shown in Fig. 11 (bottom plot), where strong and weak horizontal amplifications are indicated in red and blue colours, respectively. As mentioned above, Station1 used as a reference site to measure mean *SR* was not located on rock but on a very thin loess cover. This prevents a reliable comparison between measured and computed rates of amplifications. Therefore, in the following, focus is on resonance frequencies.

Fig. 11(b) displays the horizontal accelerations computed every 20 m along the ground surface. From this figure, it can be seen that, in areas characterized by geological layering, mainly on the left-hand side of the toe and on the right-hand side of the crest, the amplitude and duration of ground motions are enhanced because of the multiple phases generated along the interfaces among different materials and trapped in the low-velocity surface layers. The bottom plot shows that computed spectral horizontal amplifications fluctuate widely from point to point along the slope. The strongest amplification (with a factor of 6) is found at the crest of the slope, for a frequency of 3 to 4 Hz. In the middle of the slope, there is hardly any amplification whereas at the bottom of the slope, spectral amplifications are between 3.5 and 4.5 for frequencies in the range 4–5 Hz. This complex pattern of spectral horizontal amplifications is consistent with variations in loess thickness, as stated in the paragraph describing the characteristics of earthquake recordings. This result suggests that geophysical and seismological measurements resulted in an accurate representation of the slope geometry and geology.

To provide further insight into site effects distribution over the Kainama site, we also computed spectral horizontal amplifications at depth for given frequencies and especially for those for which large spectral amplifications are computed in different parts of the slope, according to Fig. 11. We focused on the near-surface since deeper amplifications are negligible (smaller than the value 1 corresponding to reference motions). The results are illustrated in Figs 12(a)–(c) for frequencies of 2.0, 3.5 and 4.5 Hz, respectively. Apart from the top plot (Fig. 12a), which confirms that amplifications below 2.5 Hz are very small, the two other plots show that
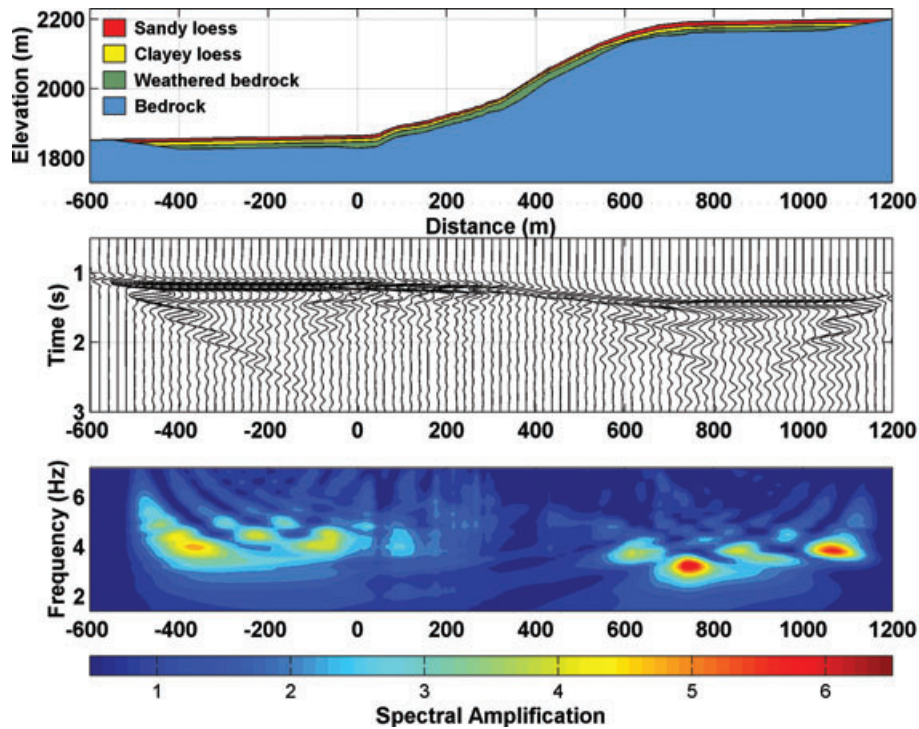
Figure 11. (a) Schematic representation of the topography and the geology of Kainama slope. (b) Horizontal accelerations computed every 20 m along the ground surface. (c) Spectral horizontal amplifications (see colour scale) computed along the ground surface.

amplifications are fairly shallow and restricted to loess deposits, which is in favour of a superficial failure in the weakest materials of the slope (loess deposits).

Modelling of slope stability in dynamic conditions

From the field observations and measurements arise many questions regarding the origin of the Kainama failure. Focusing on two possible triggering mechanisms, a seismic origin related to site effects and an activation resulting from complex phenomena involving both seismic shaking and groundwater flow, we conducted dynamic slope stability analyses with FLAC software, considering two different saturation scenarios. First, we consider a reference scenario in which the slope is dry. And, a more realistic scenario, based on electrical tomography measurements in which the slope is partially saturated with a perched groundwater table located between the base of clayey loess deposits and 2 m above the base of sandy loess deposits.

All simulations were conducted in small strain mode: the position of the nodes of the grid was not updated during the calculation process; however, some nodes could exhibit very large displacements.

Reference scenario (dynamic and dry conditions)

In this scenario, all layers are assigned the classical Mohr–Coulomb failure criterion (linear elastic–perfectly plastic). After the propagation of a 5 s long seismic signal inside the slope, additional time steps are executed to allow detection of permanent deformations in the slope. Fig. 13(a) displays the total accumulated shear strains induced by seismic shaking: zones coloured in red indicate areas where intense irreversible deformations develop, whereas blue zones stand for areas where at most elastic deformations are com-

puted. From Fig. 13(a), it can be seen that small and localised plastic shear strains develop in a non-flat zone below the crest, they are attributed to the presence of site effects (see bottom plot in Fig. 11). However, under dynamic conditions and for a dry slope, instability only occurs for PGA exceeding $0.2\,g$ (Fig. 14), a value well above the seismic shaking that preceded Kainama failure. Even in these very unlikely conditions, the contours of horizontal displacements displayed in Fig. 14(b) show that the movement of the slope is minimal (<12 mm), contrary to field observations.

The more 'realistic' scenario (dynamic and wet conditions)

The literature review of other loess sites revealed that sandy loess deposits comparable to those of Kainama slope may suffer irrecoverable volume contraction of the matrix of grains, when subjected to seismic loading. The volume of the void space decreases mainly due to grain rearrangement. If the voids are filled with water, then the pressure of the water increases (since the time needed for water to flow is much larger than the duration of one cycle of the seismic shaking). This results in a decrease of effective stresses acting on the matrix of grains and, consequently, a reduction of the soil shear strength, which may induce liquefaction.

To model this behaviour with FLAC software, we used Finn model, based on the classical Mohr–Coulomb failure criterion, incorporating the formula from Byrne (1991), which relates the decrease of the volume of the void space to cyclic shear strain amplitude:

$$\Delta\varepsilon_{\mathrm{vd}} = C_1 \cdot \gamma \cdot \exp[-C_2 \cdot \varepsilon_{\mathrm{vd}}/\gamma], \qquad (1)$$

where $\Delta\varepsilon_{\mathrm{vd}}$ is the increment of volume decrease, γ represents the cyclic shear strain amplitude and C_1 and C_2 are constants.

Considering the irreversible volume change, FLAC takes care of pore pressure build-up and decrease in effective stresses. Byrne
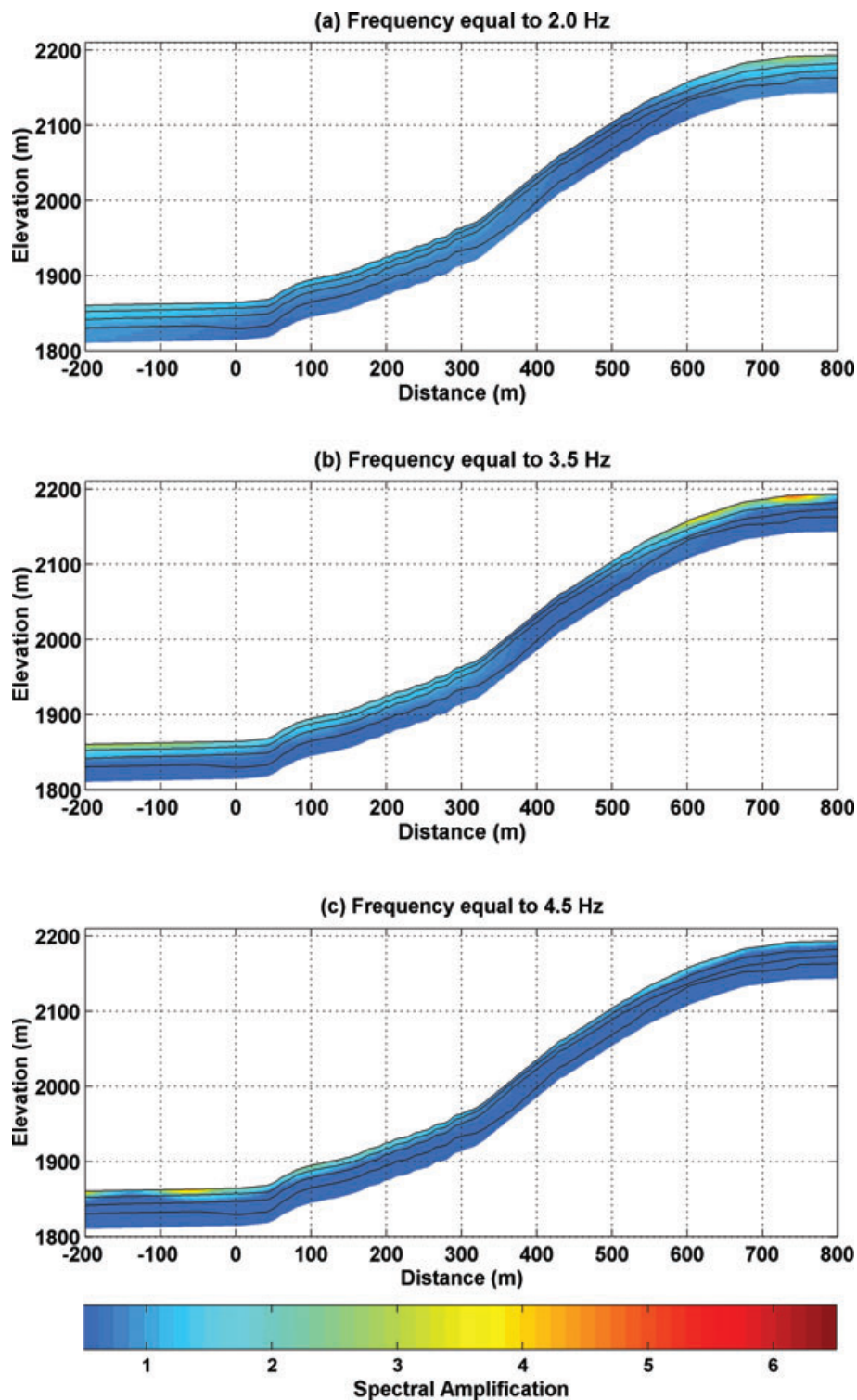
Figure 12. Spectral amplifications (see colour scale) computed over Kainama slope for frequencies of (a) 2.0, (b) 3.5 and (c) 4.5 Hz.

(1991) noted that constant C_1 can be derived from normalized standard penetration test values $(Nl)_{60}$:

$$C_1 = 8.7 \cdot [(Nl)_{60}]^{-1.25} \tag{2}$$

Constant C_2 is, in many cases, equal to $C_1/0.4$ (Byrne 1991).

The classical methods are based on the widely accepted cyclic-stress approach, with input parameters readily obtainable from routine field investigations. The Finn model, which generates pore

pressure through the contraction of the soil skeleton (real physical process), is more complicated since it requires two sets of material properties. One set, the constants C_1 and C_2, relates cyclic strain to contraction; a second set, the bulk modulus of the soil and the bulk modulus used for water, relates contraction to pore pressure generation.

The logic of the Finn model is based on strain cycles: as soon as a shear strain reversal is detected in an element, the cyclic shear
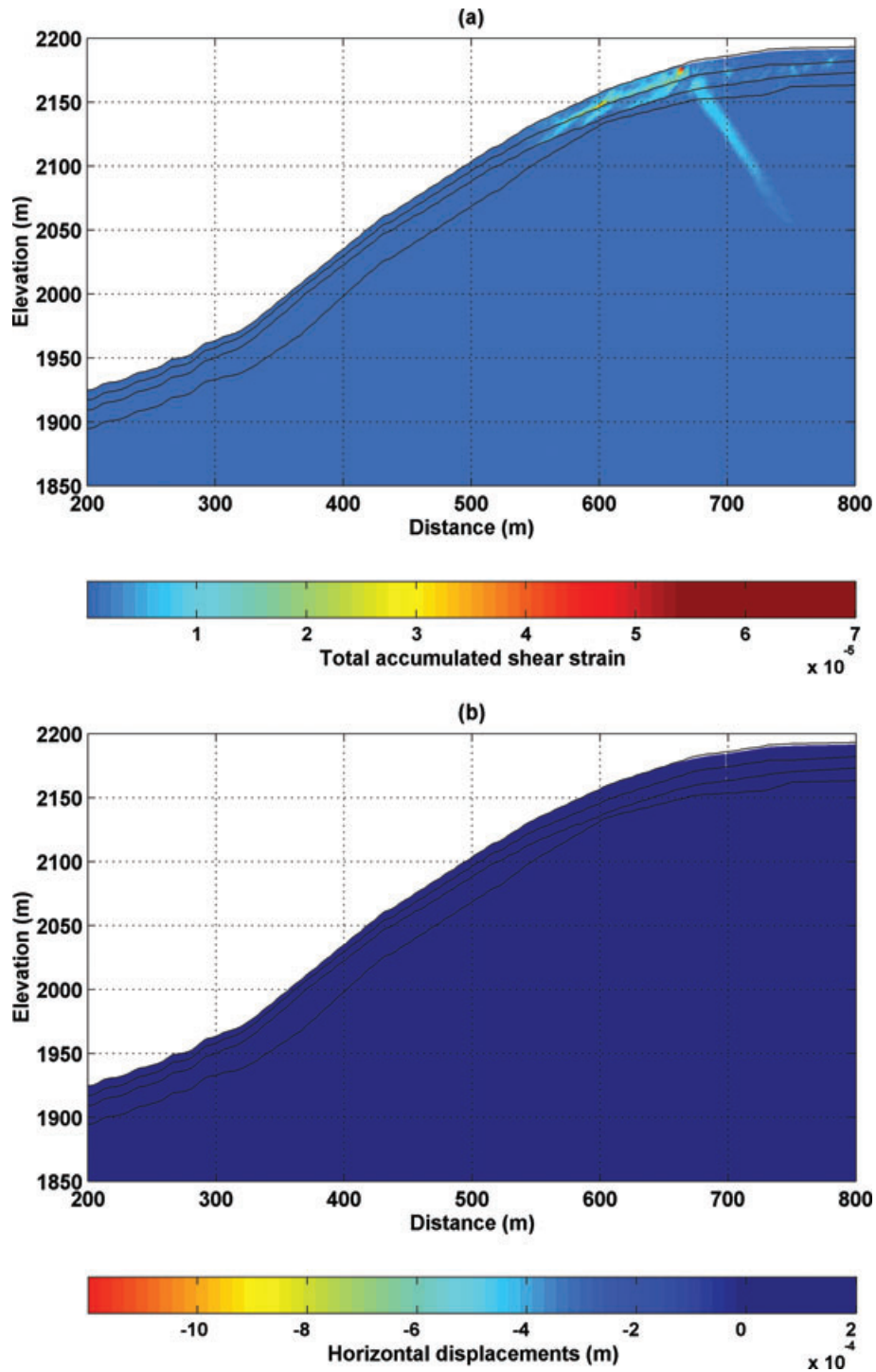
Figure 13. Total accumulated shear strains (a) and permanent displacements (b) inside the dry slope at the end of the simulation.

strain amplitude is evaluated and inserted into eq. (1) to obtain the increment in volume decrease $\Delta\varepsilon_{vd}$. The accumulated irrecoverable volume strain, ε_{vd}, is then updated as follows ($\varepsilon_{vd} := \varepsilon_{vd} + \Delta\varepsilon_{vd}$) and saved for use in eq. (1). Finally, the increment in pore pressure connected with the increment in volume decrease, $\Delta\varepsilon_{vd}$, is calculated using the bulk modulus of the soil and the bulk modulus of water.

There are two numerical parameters defined by the user, which control strain cycles detection. First, a new strain cycle may be detected, provided a minimum number of time steps has elapsed since the latest strain reversal. Second, eq. (1) is invoked only when the shear strain amplitude is larger than a limiting shear strain amplitude below which volumetric strain is not produced.

The Finn model was applied to sandy loess deposits, considering a value of 10 for $(Nl)_{60}$. This value was derived from empirical formula relating shear wave velocity to $(Nl)_{60}$ (Sykora 1987; Robertson *et al.* 1992; Youd *et al.* 1997). The other layers were assigned the classical Mohr–Coulomb failure criterion.
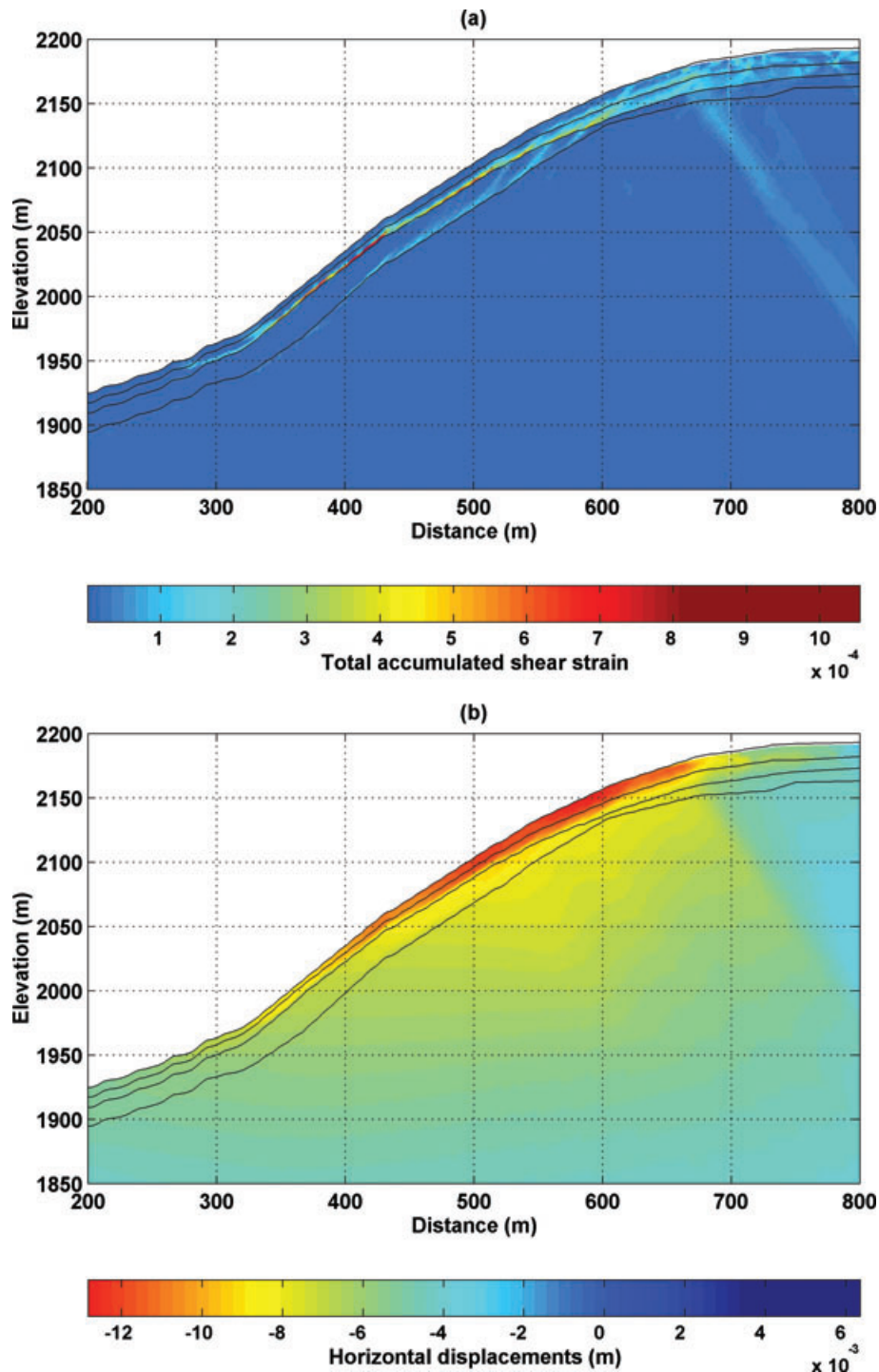
Figure 14. Total accumulated shear strains (a) and permanent displacements (b) inside the dry slope at the end of the simulation. The input PGA was linearly multiplied by a factor of 8. Note that the scales of these two plots are different from the ones of Figs 13 and 15.

While modelling slope stability in dynamic and wet conditions, we found that plastic shear strains resulting from the propagation of a 5 s long seismic signal are significantly larger than those computed in the dry slope (compare Figs 15a and 13a). They induce small permanent displacements spanning the entire slope, although the largest displacements develop uphill (Fig. 15b). However, these computed displacements (mm) are still several orders of magnitude smaller than the observed displacements (several hundreds of metres).

Time histories of horizontal acceleration, internal volume strain, pore pressure and mean effective stress at two different locations of the liquefiable layer (points A and B shown in the inset plot of Fig. 16) are shown in Fig. 16. From this figure, it can be seen that, at both locations, pore pressures build up (Fig. 16c) because of a decrease in the volume of the void space (Fig. 16b). This behaviour is more pronounced at the uppermost location, where larger horizontal accelerations (Fig. 16a) and spectral amplifications (Fig. 11) were modelled. From our results, we infer that the
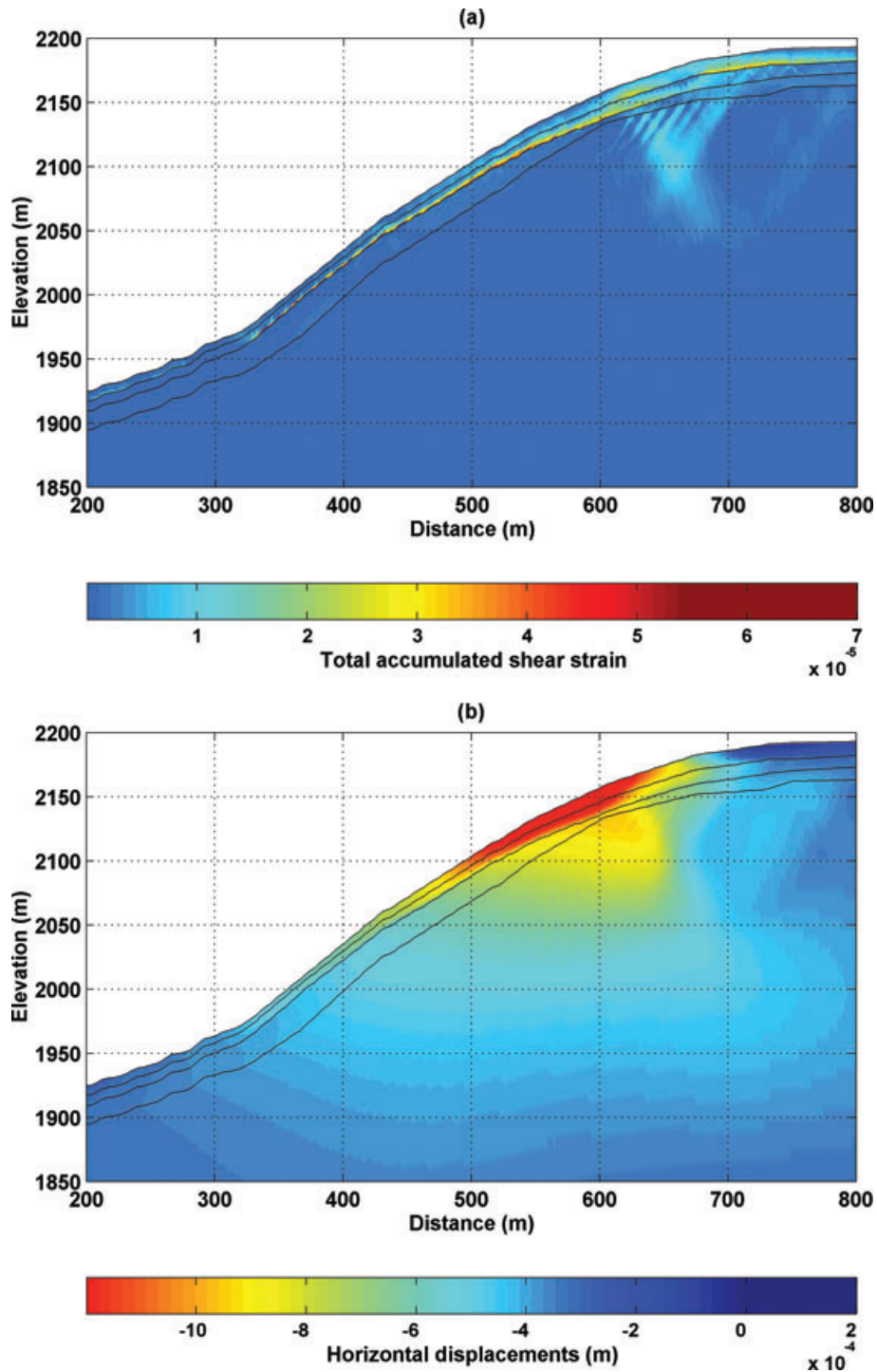
(a)

(b)

Figure 15. Total accumulated shear strains (a) and permanent displacements (b) inside the wet slope at the end of the simulation.

pore pressure generation process is, to a certain extent, linked to site effects distribution. After shaking has stopped, the ratio of excess pore pressure generated due to cyclic loading to initial static vertical effective stress, also called pore pressure ratio, is equal to 0.05 at location A and 0.26 at location B (a value of 1 would imply 100 per cent liquefaction). Consequently, there is hardly any reduction of effective stresses at location A whereas there is a 26 per cent reduction of effective stresses at location B (Fig. 16d): this indicates that the layer does not completely liquefy; a partial liquefaction affects the upper part of the slope.

DISCUSSION AND CONCLUSIONS

This study has been carried out to better understand the conditions that led to the formation of the Kainama loess earthflow and could trigger future landslides on adjacent slopes. First, a field survey, including electrical tomography and microseismic measurements, had been organized to analyse the seismic and electric properties of the ground down to a depth of 20–50 m. Digitalization (with subsequent filtering and georeferentiation) of a topographic map allowed us to create an accurate DEM. Using the geophysical and
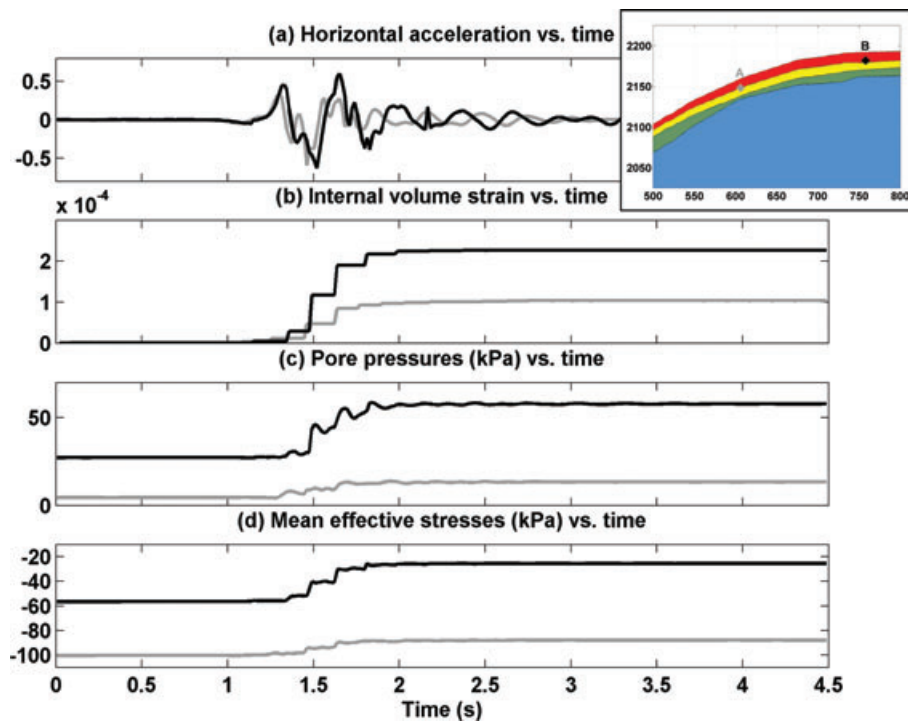
Figure 16. Time histories of horizontal acceleration, internal volume strain, pore pressure and mean effective stress at two different locations of the liquefiable layer (points A and B shown in the inset plot). In the inset plot, the different colours correspond to the different materials as defined in Fig. 11.

topographic data, a 3-D model composed of three layers has been constructed. From this model, a 2-D section along the earthflow was extracted. For the numerical modelling, the geometry and properties of the layers were defined with more detail than in the 3-D model: the basic layer was subdivided into two layers: a clayey loess layer (recognized by electrical tomography but not by microseismic measurements) on top of the weathered bedrock. The shear strength of the geological materials was derived from literature and geotechnical tests performed on sites presenting a similar loess cover. It should be outlined that the geotechnical properties, including the permeability, precise water content and normalized standard penetration test values of the geological materials as well as the level of earthquake ground motion, are affected by significant uncertainty: no tests with samples from the investigated site had been performed, and ground motions of the (assumed) triggering earthquakes had not been recorded on the site. Besides, as mentioned previously, the extension of the clayey loess layer is poorly constrained; yet, it may have a strong influence on the depth of the failure surface since it delimits the impermeable and permeable zones within the slope. Finally, we stated that soil conditions on the existent loess flow are similar to those measured on the eastern adjacent slope, but we still need to investigate why this slope, eastern adjacent of Kainama landslide, did not fail. For the reasons listed above, the present study should be considered as a parametric analysis rather than as a backanalysis. Also, the discussion will be focused on the influence of those factors on the dynamic behaviour of the ground, which were determined with a higher degree of reliability: the geometry of the layers, the groundwater level and the seismic properties of the ground.

In particular, it can be observed that field measurements and numerical computations of spectral amplifications are in fairly good agreement; they both highlight large ground motion amplifications

in areas characterized by a thick loess layer. Based on these results, we feel confident about the geometry of the layers and the values of the elastic parameters. To better understand the mechanisms that led to ground motion amplifications over the Kainama site, we plan to conduct numerical parametric studies, varying the topography and the geological layering of the slope (results will be presented in a future paper, centred on numerical modelling; in particular, we will show that topography is not prominent in the elastic response of the slope to seismic shaking).

From our numerical tests based on simplifications of the input seismic shaking, it can be seen that Kainama landslide cannot have a purely seismic origin related to site effects since the input seismic signal required to trigger a global failure of the slope is well above the hypothesized shaking of the earthquakes that preceded the triggering of the failure. Our ongoing research also demonstrates that Kainama landslide cannot have a purely static origin related to a high water table because, in this case, the sliding surface would encompass weathered bedrock and bedrock materials that were not part of the real landslide (see future paper). However, it is most likely that both seismic shaking and groundwater flow contributed to the triggering of the mass movement. Indeed, considering dynamic and wet conditions, we correctly located the failure surface, but we found that computed displacements are significantly smaller than the (possible) real displacements. The constitutive model and the shear strength parameters control the initial static slope stability and the potential modifications of materials behaviour after the onset of failure. It is clear that numerical computations with Finn model did not succeed in capturing all the mechanisms controlling slope deformations. A first reason for that may be related to the constitutive model itself—we know from experience that this model is very sensitive to minor changes in numerical and material properties. During complicated loading paths, for instance, the selection of the

threshold number of time steps to detect strain cycles may turn out to be difficult, but the user must pay attention to this parameter since it strongly controls the rate of build-up of pore pressure. Besides, we did not consider past events that could have altered the mechanical properties of the layers and, therefore, facilitated the development of large displacements within the sliding mass or the initiation of a failure for a smaller seismic shaking. We did not include softening of soils as a result of seismic shaking because simulating such a behaviour would require better constrained geotechnical data. These are weak points in our study that could be responsible for the discrepancy between observed and modelled displacements. Also, we used a relatively short-duration seismic signal with only two large peaks, which may be too conservative compared with a real longer signal. The seismic response of the slope subjected to more realistic synthetic signals, based on the source mechanism, the distance to the epicentre (influence of the angle of incidence) and the magnitude of the earthquakes that occurred prior to the triggering of the landslide is currently being investigated along with other more complex scenarios (increase of the water table level after seismic shaking to account for the heavy precipitations that followed the earthquakes). These developments will be presented in a future paper along with other types of simulations with discrete elements, which allow better to model large displacements as those observed along the Kainama loess earthflow.

To conclude this preliminary numerical analysis of Kainama landslide, we believe that the development of the catastrophic failure is a consequence of the opening of tension cracks during the seismic shaking and their filling up with water during the heavy precipitations that followed the earthquakes. We did not manage to reproduce, numerically, such tension cracks with a PGA of 0.025 *g* but, increasing the input acceleration (or reducing materials strength), we found that contours of horizontal displacements indicate significant extension at the crest of the slope, consistent with the observed tension cracks in this area (see future paper).

ACKNOWLEDGMENTS

REFERENCES

Abdrakhmatov, K., Havenith, H.-B., Delvaux, D., Jongmans, D. & Trefois, P., 2003. Probabilistic PGA and Arias intensity maps of Kyrgyzstan (Central Asia), *J. Seism.,* **7,** 203–220.

Byrne, P., 1991. A cyclic-shear volume coupling and pore-pressure model for sand. in *Proceedings of the Second International Conference on Recent Advances in Geotechnical Earthquake Engineering and Soil Dynamics,* Paper no. 1.24, pp.47–55, St Louis, MO, 1991 March.

Capon, J., 1969. High-resolution frequency-wave number spectrum analysis, *Proc. IEEE,* **57**(8), 1408–1418.

Cundall, P.A., Hansteen, H., Lacasse, S. & Selnes, P.B., 1980. NESSI— soil structure interaction programme for dynamic and static problems. Norwegian Geotechnical Institute, Report 51508-9, December.

Demanet, D., 2000. Tomographies 2D et 3D à partir de mesures géophysiques en surface et en forage, *PhD thesis.* Liege University, Belgium.

Derbyshire, E., 2001. Geological hazards in loess terrain, with particular reference to the loess regions of China, *Earth-Sci. Rev.,* **54,** 231–260.

Dodonov, A.E., 1991. Loess of Central Asia, *Geophys. J.,* **24**(2), 185–194.

Faeh, D., Kind, F. & Giardini, D., 2001. A theoretical investigation of average H/V ratios, *Geophys. J. Int.,* **145,** 535–549.

Havenith, H.-B., Strom, A., Jongmans, D., Abdrakhmatov, K., Delvaux, D. & Tréfois, P., 2003. Seismic triggering of landslides. Part A: field evidence from the Northern Tien Shan, *Nat. Hazards Earth Sys. Sci.,* **3,** 135–149.

Havenith, H.-B., Torgoev, I., Meleshko, A., Alioshin, Y., Torgoev, A. & Danneels, G., 2006. Landslides in the Mailuu-Suu Valley, Kyrgyzstan— Hazards and Impacts, *Landslides,* **3,** 137–147.

Havenith, H.-B., Fäh, D., Polonu, U. & Roullé, A., 2007. S-wave velocity measurements applied to the seismic microzonation of Basel, Upper Rhine Graben, *Geophys. J. Int.,* **170,** 346–358.

Itasca, 2005. *FLAC Manual—Theory and Background.* Minneapolis, MN.

Jongmans, D. & Garambois, S., 2007. Geophysical investigation of landslides: a review, *Bulletin de la Société Géologique de France,* **178**(2), 101–112.

Keefer, D.K., 2002. Investigating landslides caused by earthquakes—a historical review, *Surv. Geophys.,* **23,** 473–510.

Kuhlemeyer, R. L. & J. Lysmer. 1973. Finite element method accuracy for wave propagation problems. *J. Soil Mech. Found. Div.,* **99**(SM5), 421– 427.

Lebourg, T., Binet, S., Tric, E., Jomard, H. & Bedoui, S. E., 2005. Geophysical survey to estimate the 3D sliding surface and the 4D evolution of the water pressure on part of a deep seated landslide, *Terra Nova,* **17**(5), 399–406.

Leonov, N.N., 1960. The Khait, 1949 earthquake and geological conditions of its origin. in *Proceedings of the Academy of Sciences of the USSR, Geophys. Series 3* (in Russian), pp. 409–424.

Loke, M. H. & Barker, R. D., 1996. Rapid least-squares inversion of apparent resistivity pseudosections by a quasi-Newton method, *Geophys. Prospect.,* **44,** 131–152.

Lysmer, J. & Kuhlemeyer, R.L., 1969. Finite dynamic model for infinite media, *J. Eng. Mech.,* **95**(EM4), 859–877.

Meric, O., Garambois, S., Malet, J.-P., Cadet, H., Guéguen, P. & Jongmans, D., 2007. Seismic noise-based methods for soft-rock landslide characterization, *Bulletin de la Société Géologique de France,* **178**(2), 137– 148.

Nakamura, Y., 1989. A method for dynamic characteristics estimation of subsurface using microtremor on the ground surface, *Quart. Rept. RTRI,* **30,** 25–33.

Ohrnberger, M., 2004. User manual for software package CAP—a continuous array processing toolkit for ambient vibration array analysis, SESAME report D18.06, available at http://sesamefp5.obs.ujf-grenoble.fr.

Perrone, A., Iannuzzi, A., Lapenna, V., Lorenzo, P., Piscitelli, S., Rizzo, E. & Sdao, F., 2004. Highresolution electrical imaging of the Varco d'Izzo earthflow (southern Italy), *J. appl. Geophys.,* **56,** 17–29.

Plafker, G., Erickson, G.E. & Concha, J.F., 1971. Geological aspects of the May 31, 1970, Peru earthquake, *Bull. Seism. Soc. Am.,* **61,** 543–578.

Pye, K., 1995. The nature, origin and accumulation of loess, *Quat. Sci. Rev.,* **14,** 653–667.

Robertson, P.K., Woeller, D.J. & Finn, W.D.L., 1992. Seismic cone penetration test for evaluating liquefaction potential under cycling loading, *Can. Geotech. J.,* **29,** 686–695.

Roessner, S., Wetzel, H.-U., Kaufmann, H. & Sarnagoev, A., 2005. Potential of satellite remote sensing and GIS for landslide hazard assessment in Southern Kyrgyzstan (Central Asia), *Nat. Hazards,* **35,** 395–416.

Strom, A. L. & Korup, O., 2006. Extremely large rockslides and rock avalanches in the Tien Shan Mountains, Kyrgyzstan, *Landslides,* **3**(2), 125–136.

Sykora, D.W., 1987. Creation of a database of seismic shear wave velocities for correlation analysis, Geotechnical Laboratory Miscellaneous Paper GL-87–22, U.S. Army Engineer Waterways Experiment Station, Vicksburg, MS.

Wathelet, M., 2005. Array recordings of ambient vibrations: surface-wave inversion, *PhD thesis.* Liege University, Belgium.

Wathelet, M., Jongmans, D. & Ohrnberger, M., 2004. Surface wave inversion using a direct search algorithm and its application to ambient vibration measurements, *Near Surf. Geophys.,* **2,** 211–221.

Youd, T.L. *et al.*, 1997. Summary report, NCEER Workshop on evaluation of liquefaction resistance of soils, Technical report NCEER-97-0022, pp.1–40, Salt Lake City, UT, National Center for Earthquake Engineering Research, Buffalo, NY, 1996 January 4–5.

Zhang, Z. & Lanmin, W., 1995. Geological disasters in loess areas during the 1920 Haiyuan Earthquake, China, *Geophys. J.,* **36**(2), 269–274.